BRDF correction of S3 OLCI water reflectance products

EUMETSAT Contract Ref.: RB_EUM-CO-21-4600002626-JIG

Algorithm Theoretical Basis Document

Final version

16 January 2023

TABLE OF CONTENTS

LIST OF ACRONYMS AND ABBREVIATIONS

ADF	Ancillary Data File
AERONET	AErosol RObotic NETwork
AERONET-OC	Ocean Color component of the Aerosol Robotic Network
AOP	Apparent Optical Properties
AOT	Atmospheric Optical Thickness
ATBD	Algorithm Theoretical Basis Document
ATM	Inherent optical properties of the atmosphere
BRDF	Bidirectional Reflectance Distribution Function
BRDF-BS	BRDF-"Benchmark Studies"
Cal/Val	Calibration and Validation
CDOM	Colored Dissolved Organic Matter
DPM	Detailed Processing Model document
EC	European Commission
ESA	European Space Agency
EU	European Union
EUMETSAT	European Organisation for the Exploitation of Meteorological Satellites
FCI	Flexible Combined Imager
FRM4SOC	Fiducial Reference Measurements for Satellite Ocean Colour
GSFC	Goddard Space Flight Center
HPLC	High-Performance Liquid Chromatography
IOCCG	International Ocean Colour Coordinating Group
IODD	Input Output Data Definition Document
IOP	Inherent Optical Property
IPF	Instrument Processing Facility
L11	(Lee et al., 2011), one of the BRDF methods
L1B	Level 1 B
L2	Level 2
LUT	Look Up Table
M02	(Morel et al., 2002), one of the BRDF methods
MDB	Matchup Database
MERIS	MEdium Resolution Imaging Spectrometer
MOBY	Marine Optical Buoy
MTG	Meteosat Third Generation
NAP	Non-Algal Particles
NASA	National Aeronautics and Space Administration
NIR	Near Infrared
OAA	Observation azimuth angle
OC	Ocean Colour
OCI	Ocean Color Instrument

OC-SAC	Ocean Colour Standard Atmospheric Correction
OFS	Optical Floating System
OLCI	Ocean and Land Colour Imager
OZA	Observation azimuth angle
P05	(Park and Ruddick, 2005), one of the BRDF methods
PACE	Plankton, Aerosol, Cloud, ocean Ecosystem
RD	Reference Documents
RT	Radiative Transfer
RTC	Radiative Transfer Code
RTE	Radiative Transfer Equation
RTM	Radiative Transfer Model
S3	Sentinel-3
SNR	Signal-to-Noise Ratio
SoW	Statement of Work
SVC	System Vicarious Calibration
SZA	Sun zenith angle
T18	(Twardowski and Tonizzo, 2018), one of the BRDF methods
TOA	top-of-the-atmosphere
TSM	Total Suspended Matter
VIIRS	Visible Infrared Imaging Radiometer Suite
VIS	VISible domain of the solar spectrum
VSF	Volume Scattering Function

LIST OF SYMBOLS

$\boldsymbol{a}$	Absorption coefficient [m^{-1}]
$\boldsymbol{\Delta\phi}$	Angle between the viewing and sun azimuth [deg.]
$\boldsymbol{K_\infty}$	Asymptotic attenuation coefficient
$\boldsymbol{V}$	Atmospheric horizontal visibility [km]
$\boldsymbol{c}$	Attenuation coefficient [m^{-1}]
$\boldsymbol{K_{Lu}}$	Attenuation coefficient for upwelling radiance
$\boldsymbol{\bar{\mu}_\infty}$	Average cosine of the asymptotic light field
$\boldsymbol{b_b}$	Back Scattering coefficient [m^{-1}]
$\boldsymbol{B_p}$	Backscattering ratio
$\boldsymbol{\tilde{b}_b}$	Backscattering ratio (also expressed as B_p)
$\boldsymbol{B_{NAP}}$	Backscattering ratio for non-algal particles
$\boldsymbol{B_{ph}}$	Backscattering ratio for phytoplankton
$\boldsymbol{C}$	BRDF correction factor (also used for chlorophyll-a concentration)
Chl	Chlorophyll-a concentration (also expressed as C)
$\boldsymbol{\Re}$	Coefficient accounting for transmission and reflection effects at the sea surface
$\boldsymbol{a_{cdm}}$	Colored dissolved matter absorption coefficient [m^{-1}]
$\boldsymbol{a_{CDOM}}$	Colored dissolved organic matter absorption coefficient [m^{-1}] (a_g is also used)
$\boldsymbol{\mu_S}$	Cosine of the solar zenith angle
$\boldsymbol{K_d}$	Diffuse attenuation coefficient
$\boldsymbol{E_d}$	Downward irradiance [Wm^{-2} nm^{-1}]
$\boldsymbol{0^+}$	Elevation just above the sea surface [m]
$\boldsymbol{\rho_w^{ex}}$	Exact water reflectance
$\boldsymbol{\theta_s'}$	In-water sun zenith angle [deg.]
$\boldsymbol{R}$	Irradiance reflectance
$\boldsymbol{F_0}$	Mean extraterrestrial solar spectral irradiance [W m^{-2} nm^{-1}]
$\boldsymbol{a_{nap}}$	Non-algal particle absorption coefficient [m^{-1}] (a_{NAP} is also used)
$\boldsymbol{b_{bNAP}}$	Non-algal particle backscattering coefficient [m^{-1}]
$\boldsymbol{a_{nw}}$	Non-water absorption coefficient [m^{-1}]
$\boldsymbol{r_{rs,n}}$	Normalized underwater reflectance [sr^{-1}]
$\boldsymbol{L_{nw}}$	Normalized water-leaving Radiance [Wm^{-2} sr^{-1} nm^{-1}]
$\boldsymbol{\tau}$	Optical thickness of atmospheric constituents (also expressed as τ_a)
$\boldsymbol{a_p}$	Particle absorption coefficient [m^{-1}]
$\boldsymbol{c_p}$	Particle attenuation coefficient [m^{-1}]
$\boldsymbol{b_{bp}}$	Particle backscattering coefficient [m^{-1}]
$\boldsymbol{a_{phy}}$	Phytoplankton absorption coefficient [m^{-1}] (a_{ph} is also used)
$\boldsymbol{c_{ph}}$	Phytoplankton attenuation coefficient [m^{-1}]
$\boldsymbol{b_{bph}}$	Phytoplankton backscattering coefficient [m^{-1}]

$\Psi_{K_{L_u}}$	Ratio of diffuse upwelling attenuation coefficient to the asymptotic attenuation coefficient
η_b	Ratio of pure water to total backscattering (η_{bb} is also used)
Q	Ratio of the upward irradiance to directional upward radiance
$\mathbf{R_{rs}}$	Remote Sensing reflectance [Wm^{-2} nm^{-1}]
Ψ	Scattering angle [deg.]
b	Scattering coefficient [m^{-1}]
$\widetilde{\omega}$	Single scattering albedo
θ_s	Sun zenith angle [deg.]
r_{rs}	Underwater reflectance [sr^{-1}]
E_u	Upward irradiance [Wm^{-2} nm^{-1}]
L_u	Up-welling radiance [Wm^{-2} sr^{-1} nm^{-1}]
f_L	Upwelling radiance shape factor
Ω	Viewing and illumination geometry
Ω_o	Viewing and illumination geometry
β	Volume scattering function
b_{bw}	Water backscattering coefficient [m^{-1}]
ρ_w	Water reflectance
L_w	Water-leaving Radiance [Wm^{-2} sr^{-1} nm^{-1}]
λ	Wavelength[nm]
W	Wind speed [ms^{-1}] (W is also used)
y	Yellow substance / Colored dissolved organic matter
θ_v	Zenith angle of the viewing direction [deg.]

LIST OF FIGURES

LIST OF TABLES

1 OVERVIEW

The Algorithm Theoretical Basis Document (ATBD) presents methodological and operational elements of the study "BRDF correction of S3 OLCI water reflectance products" commissioned by EUMETSAT. As a general concept, the Bidirectional Reflectance Distribution Function (BRDF; Bartell et al., 1981) describes angular reflection properties. If the illuminated area were opaque such as dry land, the BRDF effect would be driven only by the optical characteristics of the reflecting surface. In the ocean, the BRDF also depends on the optical properties of the illuminated volume, and different factors can cause radiance anisotropy. It is then necessary taking BRDF effects into account to minimize the dependence of the measured water reflectances on any factor that is not an Inherent Optical Property (IOP) of seawater, and by this means improving the quality of ocean color data products.

Different BRDF correction schemes have been presented in the literature for ocean color applications, as reviewed in the Requirement Baseline Document (deliverable RB_EUM-CO-21-4600002626-JIG_V2.0.docx) of this study. The reference ones are those proposed by

- Morel et al. (2002), henceforth designated as M02;
- Park and Ruddick (2005), designated as P05;
- Lee et al. (2011), designated as L11;
- He et al. (2017), designated as H17;
- Twardowski and Tonizzo (2018), designated as T18—the original study denotes this scheme as ZTT for Zaneveld-Twardowski-Tonizzo (Zaneveld, 1995).

The RB analysis showed that the H17 method has limited spectral applicability and was excluded from further evaluations. The performance of the M02, P05 and L11 BRDF correction methods is documented in the Product Validation Report (PVR, deliverable PVR_EUM-CO-21-4600002626-JIG_V3.0.docx), and validation results are summarized in this document. Since T18 is still under revision, only its methodological aspects are henceforth considered without references to applicative results. Topics addressed in the ATBD are the following:

- BRDF principles and their formulation in different correction schemes (Sec. 2),
- BRDF correction applicability (Sec. 3),
- BRDF correction uncertainty (Sec. 4),
- implementation of the BRDF module Sec. (5), and
- guidelines for future development (Sec. 6).

2 BRDF METHODS

This section presents the following methodological aspects:

- general BRDF principles and
- details on specific BRDF formulations.

2.1 METHODS REVIEW

The Bidirectional Reflectance Distribution Function (BRDF; Bartell et al., 1981) is mathematically defined as the spectral ratio of the differential reflected radiance $\mathrm{d}L_r(\lambda, \theta_\mathrm{i}, \phi_\mathrm{i}, \theta_\mathrm{r}, \phi_\mathrm{r})$ to the differential incident irradiance $\mathrm{d}E_\mathrm{i}(\lambda, \theta_\mathrm{i}, \phi_\mathrm{i})$

$$\mathrm{BRDF} = \frac{\mathrm{d}L_r(\lambda, \theta_\mathrm{i}, \phi_\mathrm{i}, \theta_\mathrm{r}, \phi_\mathrm{r})}{\mathrm{d}E_i(\lambda, \theta_\mathrm{i}, \phi_\mathrm{i})} = \frac{\mathrm{d}L_r(\lambda, \theta_\mathrm{i}, \phi_\mathrm{i}, \theta_\mathrm{r}, \phi_\mathrm{r})}{L_i(\lambda, \theta_\mathrm{i}, \phi_\mathrm{i})\cos(\theta_\mathrm{i})\,\mathrm{d}\omega_\mathrm{i}}, \quad (1)$$

where θ and ϕ are the zenith and azimuth angles, respectively; the subscripts r and i are the reflected and incident fluxes, respectively; and ω indicates the solid angle (see the Appendix for a description of radiometric quantities).

In the framework of ocean color remote sensing, the BRDF effect of primary interest is related to changes in the water reflectance $\rho_w(\lambda, \theta_\mathrm{s}, \theta_\mathrm{v}, \Delta\phi)$ as a function of the sun zenith angle θ_s, the viewing zenith angle θ_v, and the relative azimuth angle between the sun and the observer $\Delta\phi$. The scope of the BRDF correction is to minimize these ρ_w variations. In this respect, Morel and Gentili (1996) gave the following definition of the fully (or exact) normalised water reflectance: the reflectance that a nadir-viewing instrument would measure if the sun were at the zenith, in the absence of any atmospheric loss and when the Earth is at its mean distance from the sun.

The angular illumination and viewing geometry can be expressed as $\Omega = (\theta_\mathrm{s}, \theta_\mathrm{v}, \Delta\phi)$, using the "o" index Ω_o for the nadir view and the sun at the zenith—the latter also indicated as $\rho_w^{ex}(\lambda)$. The BRDF correction factor to transform $\rho_w(\lambda, \Omega)$ into $\rho_w(\lambda, \Omega_\mathrm{o})$ is

$$C(\lambda, \Omega, \mathrm{ATM}, W, \mathrm{IOP}) \equiv \frac{\hat{\rho}_w(\lambda,\ \Omega_\mathrm{o}, \mathrm{ATM}, W, \mathrm{IOP})}{\hat{\rho}_w(\lambda, \Omega, \mathrm{ATM}, W, \mathrm{IOP})}, \quad (2)$$

where:

- the circumflex indicates modelled quantities, and
- IOP and ATM represent the inherent optical properties of the seawater and the atmosphere, respectively, and W is the wind speed—note that the wavelength dependence of these terms has been omitted in Eq (2).

Assuming C known—*i.e.*, computed as a solution of the Radiative Transfer Equation (RTE) or derived with a Radiative Transfer Model (RTM) such as Hydrolight simulations (Mobley, 1994; Mobley et al., 2021)—the BRDF-correction equation to derive the exact water reflectance $\rho_\mathrm{w}^\mathrm{ex}(\lambda)$ from the actual measurement $\rho_w(\lambda, \Omega)$ is then

$$\rho_w^{ex}(\lambda) = \rho_w(\lambda, \Omega_\mathrm{o}) \equiv \rho_w(\lambda, \Omega) C(\lambda, \Omega, \mathrm{ATM}, W, \mathrm{IOP}). \quad (3)$$

In the operational processing of OLCI data, IOPs need to be estimated from $\rho_w(\lambda, \Omega)$ and ATM from the upstream atmospheric correction. Rather than the capability to model accurately $\hat{\rho}_w^{ex}(\lambda)$ and $\hat{\rho}_w(\lambda, \Omega)$, the main requirement for the C-tables construction is that the ratio between nadir and off-nadir values is adequately considered. Note that some uncertainties in the modelled water reflectances $\hat{\rho}_w^{ex}(\lambda)$ and $\hat{\rho}_w(\lambda, \Omega)$—for instance, spectral shapes—may cancel out with the ratio.

With reference to BRDF correction methods presented in the literature, the M02 scheme (Morel et al., 2002; Morel and Gentili, 1996, 1993) is focused on applications in Case 1 waters by

parametrizing seawater optical properties through the Chlorophyll-a concentration (*Chl*). However, the radiative transfer component embedded in M02 is not constrained to Case 1 waters, as discussed later in this document. Studies to extend the BRDF correction to waters with increased optical complexity include the P05, L1, and T18 models. These approaches determine BRDF correction coefficients based on IOPs instead of *Chl*.

On the BRDF correction implementation side, two primary approaches have been considered:

1. relying on numerical simulations and applying a specific fit to the relationship $R_{rs} = \mathrm{F}\left(\frac{b_b}{a}\right)$, or $R_{rs} = \mathrm{F}\left(\frac{b_b}{a+b_b}\right)$, as in M02, P05, and L11, or
2. approximating the RTE with an analytical formulation explicitly dependent on the VSF, as in T18.

The following sections specify elements underpinning each method (see Table 1).

Table 1 Overview of the IOP models to perform radiative transfer simulations.

		Analytical approach			
		M02	**P05**	**L11**	**T18**
AOP models		AOP tabulated from Hydrolight simulations at 412.5, 442.5, 490, 510, 560, 620, and 660 nm The spectral range in the revision by B. Gentili is 350–700 nm	AOP fitted from Hydrolight simulations at 412, 443, 490, 510, 555, 565, 620, 665, 710, and 780 nm	AOP fitted from Hydrolight simulations generated between 400 and 800 nm at 10 nm step	AOPs mainly derived through analytical modeling. Note that some modeling parts are from Hydrolight simulations at various spectral ranges.
IOP models	$\boldsymbol{a}$	a (Morel and Maritorena, 2001)	a_{w} (Pope and Fry, 1997), (Smith and Baker, 1981) $a_{\mathrm{ph}}, a_{CDOM}, a_{NAP}$ (Bricaud et al., 1998)	a_{w} (Pope and Fry, 1997) a_{ph} a_{CDOM} a_{NAP} (*IOCCG*, 2006)	a_{w} (Pope and Fry, 1997) a_{ph} (Ciotti et al., 2002) a_{CDOM} (Twardowski et al., 2004) a_{NAP} (Roesler and Perry, 1995)
	$\boldsymbol{b_b}$	$b_{b\mathrm{w}}$ (Morel, 1974) $b_{b\mathrm{p}}$ (Loisel and Morel, 1998)	$b_{b\mathrm{w}}$ (Morel, 1974) $b_{b\mathrm{p}}$ (Ulloa et al., 1994), (Twardowski et al., 2001), (Haltrin et al., 2002)	$b_{b\mathrm{w}}$ (Morel, 1974) $b_{b\mathrm{p}}$ (*IOCCG*, 2006)	$b_{b\mathrm{w}}$ (Zhang et al., 2009) $b_{b\mathrm{p}}$ (Loisel and Morel, 1998)
	VSF	Large and small population phase functions with backscattering efficiency of 0.19% and 1.4%, blended according to *Chl*	Two Fournier-Forand (Fournier, 2007; Fournier and Forand, 1994) with backscattering efficiency of 3% and 0.2% blended according to *Chl*	The Petzold (1972) average phase function, scaled with the concentration of non-algal material and a 1% backscattering efficiency Fournier-Forand (Fournier, 2007; Fournier and Forand, 1994), scaled with *Chl*	Generic (input of the model) Volume Scattering Function obtained as best fit against measurements found with the single spectrally constant function after (Sullivan and Twardowski, 2009)

2.2 BRDF FORMULATION BASED ON FITTING MODELED WATER REFLECTANCES

2.2.1 The "Morel et al." BRDF scheme (M02)

The M02 approach determines the BRDF correction factors through the typical Case 1 waters relationship between *Chl* and IOPs. This formulation can lower the BRDF correction performance as the optical complexity increases. Nonetheless, the association between IOPs and BRDF effects embedded in the M02 look-up tables (LUT) is based on radiative transfer modelling. It is hence general in its principles upon assuming as appropriate the Volume Scattering Function (VSF) and the optical variability. What bounds the applicability of this BRDF correction to Case 1 waters is the *Chl* dimension of the LUT.

M02 relies on a detailed characterization of the VSF by considering the variability of the particle size distribution as a function of *Chl*. The ocean colour community has extensively applied the M02 scheme for the BRDF correction of both satellite and in-situ data (Mobley et al., 2016). The M02 model also implicitly includes Raman scattering by deriving the LUT from RT simulations results where this effect was considered. Note that M02 is a two-step iterative scheme: 1) the R_{rs} spectrum is employed to estimate the *Chl* value, and 2) the retrieved *Chl* value is applied to determine the BRDF correction coefficient from the LUT and recompute the R_{rs} spectrum. Iteration continues until converging. This procedure ensures complete consistency between *Chl* and R_{rs} required by the BRDF correction.

The M02 expression of the "exact" water reflectance $\rho_{\mathrm{w}}^{\mathrm{ex}}$ is

$$\rho_{\mathrm{w}}^{\mathrm{ex}}(\lambda) = \rho_{\mathrm{w}}(\lambda, \theta_{\mathrm{s}}, \theta_{\mathrm{v}}, \Delta\phi)\frac{\Re_{\mathrm{o}}(W)}{\Re(\theta_{\mathrm{v}}', W)}\frac{f_{\mathrm{o}}(\mathrm{ATM}, W, \mathrm{IOP})}{Q_{\mathrm{o}}(\mathrm{ATM}, W, \mathrm{IOP})}\left[\frac{f(\theta_{\mathrm{s}}, \mathrm{ATM}, W, \mathrm{IOP})}{Q(\theta_{\mathrm{s}}, \theta_{\mathrm{v}}', \phi, \mathrm{ATM}, W, \mathrm{IOP})}\right]^{-1}, \quad (4)$$

where:

- $\Re$ accounts for transmission and reflection effects at the sea surface (θ_{v}' is the in-water angle determined from the above-surface viewing direction θ_{v} with Snell's law), and
- f links the ratio of the backscattering to the absorption coefficient (b_b and a, respectively) to the irradiance reflectance R:

$$R = \frac{E_{\mathrm{u}}(0^-)}{E_{\mathrm{d}}(0^-)} \equiv f \cdot \frac{b_b}{a}, \quad (5)$$

  with E_{u} indicating the upward irradiance.

- The Q-factor is the ratio of the upward irradiance to the upward directional radiance

$$Q(\theta_{\mathrm{s}}, \theta_{\mathrm{v}}', \Delta\phi, \mathrm{ATM}, W, \mathrm{IOP}) \equiv \frac{E_{\mathrm{u}}(0^-, \theta_{\mathrm{s}}, \mathrm{ATM}, W, \mathrm{IOP})}{L_{\mathrm{u}}(0^-, \theta_{\mathrm{s}}, \theta_{\mathrm{v}}', \Delta\phi, \mathrm{ATM}, W, \mathrm{IOP})}. \quad (6)$$

  This bidirectional factor would be equal to π with a hypothetical isotropic scattering medium but is higher in practice. It can go up to a value of 6 for high *Chl* values. It also has some spectral variability and tends to increase at red wavelengths.

Original LUTs for f/Q described in the M02 paper are available at ftp://oceane.obs-vlfr.fr/pub/gentili/AppliedOptics2002/. A table revision has been formulated by B. Gentili for OLCI spectral channels (available in OLCI Level-2 Auxiliary Data Files), as well as further extension in spectral range and higher spectral resolution (350–700 nm, every 5 nm; unpublished data).

2.2.2 The "Park and Ruddick" BRDF scheme (P05)

The Park and Ruddick (2005) BRDF scheme (P05) is based on a fourth-order polynomial fitting of R_{rs} as a function of $b_b/(a+b_b)$

$$R_{rs}(\lambda,\theta_S,\theta_V,\Delta\phi)=\sum_{i=1}^{4} g_i(\lambda,\theta_s,\theta_v,\Delta\phi,\gamma_b)\left(\frac{b_b(\lambda)}{a(\lambda)+b_b(\lambda)}\right)^i \tag{7}$$

where γ_b is the particle fraction of the backscatter, *i.e.*, $\gamma_b = b_{bp}/b_b = 1-\eta_b$ with η_b indicating the ratio of pure water to total backscattering, b_{bw}/b_b. The polynomial was fitted against simulations covering Case-1 and Case-2 waters, which explains its potential genericity for all water types.

Strictly speaking, P05 is not a BRDF correction scheme because it does not provide a method to convert $R_{\mathrm{rs}}(\lambda,\Omega)$ to $R_{\mathrm{rs}}(\lambda,\Omega_{\mathrm{o}})$, *i.e.*, does not include the IOPs retrieval algorithm. Using P05 in a BRDF-correction scheme then a numerical method to retrieve IOPs, for instance, as in the POLYMER/SACSO code (Steinmetz, 2021).

The P05 LUTs are available at:
http://odnature.naturalsciences.be/remsem/software-and-data/bidirectional-water-reflectance
Note that the download address reported in the paper of Park and Ruddick (2005) is not active.

2.2.3 The "Lee et al." BRDF scheme (L11)

The L11 approach uses a second-order polynomial of the IOP ratios to model R_{rs}. The particularity of this formulation is the explicit separation between molecular and particle scattering. The motivation for this is that $\frac{b_b}{a+b_b}$ is ambiguous regarding the angular variation of the light field because of the different phase functions of molecular and particle scattering.

Analytically, L11 provides the significant advantage that the model coefficients depend only on the geometry, unlike previous schemes. In addition, there it features an analytical inversion scheme to retrieve the IOPs from the water reflectance. These IOPs are univocal for all geometries, and therefore, R_{rs} can be recalculated at any other geometry by using the model in forward mode. The remote sensing reflectance is computed as:

$$\begin{aligned} R_{rs}(\lambda,\theta_s,\theta_v,\Delta\phi) &= \left(G_0^w(\theta_s,\theta_v,\Delta\phi)+G_1^w(\theta_s,\theta_v,\Delta\phi)\frac{b_{bw}(\lambda)}{a(\lambda)+b_b(\lambda)}\right)\frac{b_{bw}(\lambda)}{a(\lambda)+b_b(\lambda)} \\ &+\left(G_0^p(\theta_s,\theta_v,\Delta\phi)+G_1^p(\theta_s,\theta_v,\Delta\phi)\frac{b_{bp}(\lambda)}{a(\lambda)+b_b(\lambda)}\right)\frac{b_{bp}(\lambda)}{a(\lambda)+b_b(\lambda)}. \end{aligned} \tag{8}$$

L11 is a model of general applicability, from very clear to very turbid waters, therefore with the potential of replacing M02 in the latter. However, the radiative transfer simulations made to obtain the model coefficients did not consider Raman scattering, which may be a limitation *a priori* for the clearest waters. If needed, the Raman contribution needs then be removed from $R_{rs}(\lambda)$ before applying the QAA procedure (see Sec. 2.4). The phase function in L11 is a weighted average of two. One for non-algal particles modelled as the Petzold average phase function (backscattering ratio = 1.83%) and the other for phytoplankton, modelled as a Fournier-Forand phase function with a 1% backscattering ratio. The use of the Petzold PF can represent a limitation to L11 results.

The $a(\lambda)$ and $b_b(\lambda)$ values are determined with an update of the Quasi-Analytical Algorithm (QAA; Lee et al., 2002) that includes the new R_{rs} formulation (Lee et al., 2011):

- $a(560)$ is estimated as

$$\begin{cases} \chi = \log\left(\dfrac{R_{rs}(443)+R_{rs}(490)}{R_{rs}(560)+5\dfrac{R_{rs}(667)}{R_{rs}(490)}R_{rs}(667)}\right) \\ a(560) = a_w(560) + 10^{-1.146-1.366\chi-0.469\chi^2} \end{cases} \tag{9}$$

  where the absorption coefficient of pure water $a_w(560)$ is derived from Pope and Fry (1997). As one can see, $a(560)$ retrieval does not consider the geometry, which is a reasonable approximation, as to a first order, BRDF effect affect much more the R_{rs} magnitude than its shape, and eq. (8) are essentially band ratios.
- $b_{bp}(560)$ is calculated from $a(560)$ and $R_{rs}(560)$ analytically by forcing $R_{rs}(560)$, closure, which leads to a quadratic equation that is solved analytically,
- spectral $b_{bp}(\lambda)$ is the expressed as

$$b_{bp}(\lambda) = b_{bp}(560)\left(\frac{560}{\lambda}\right)^{Y} \tag{10}$$

  with

$$Y = 2.0\left(1 - 1.2e^{-0.9\frac{R_{rs}(443)}{R_{rs}(560)}}\right), \tag{11}$$

- the spectral absorption coefficient $a(\lambda)$ is further calculated from the known $b_{bp}(\lambda)$ and spectral $R_{rs}(\lambda)$ by forcing $R_{rs}(\lambda)$ closure at all bands based on Eq. (8).

2.3 BRDF FORMULATION BASED ON AN EXPLICIT DEPENDENCE ON THE VSF

2.3.1 The "Twardowski and Tonizzo" BRDF scheme (T18)

The T18 BRDF correction is based on an analytical solution of Zaneveld's restatement of the RTE (Zaneveld, 1995). The T18 formulation links R_{rs} to a, b_b and, importantly, to the VSF β by means of simplifying assumptions supported by Hydrolight simulations. The model equation is:

$$R_{rs}(\lambda,\theta_s,\theta_v,\Delta\phi,V,a,b_b) \cong \Re(\theta_V,W)\cdot \left\{ r_{rs,\mathrm{Raman}}(\lambda,\theta'_S,a,b_b) + \frac{1}{\bar{\mu}_d\left(\lambda,\theta'_s,V,\frac{b_b(\lambda)}{a(\lambda)},\eta_b\right)}\frac{\beta(\lambda,\Psi)}{b_b(\lambda)} \Big/ \left[\frac{a(\lambda)}{b_b(\lambda)}\left(1+\frac{\cos(\theta_v)\,\Psi_{K_{Lu}}(\lambda,\psi)}{\bar{\mu}_\infty\left(\frac{b_b(\lambda)}{a(\lambda)},\eta_b(\lambda)\right)}\right) + f_L(\lambda,\theta_S,\theta_V,\phi)\left(1-\tilde{b}_b^{-1}(\lambda)\right)+\tilde{b}_b^{-1}(\lambda)\right]\right\} \quad (12)$$

with $R_{rs,\mathrm{Raman}}$ derived according to Westberry et al. (2013), θ'_s is the in-water sun zenith angle, V is the atmospheric horizontal visibility that depends on Aerosol Optical Thickness (AOT) and is also the input to the Gregg and Carder (1990) model used in Hydrolight simulations, η_b is the molecular fraction of total backscattering b_{bw}/b_b, β/b_b is the scattering phase function in the backward direction, $\Psi_{K_{Lu}}$ is the ratio of the diffuse upwelling attenuation coefficient to the asymptotic attenuation coefficient K_{Lu}/K_∞, f_L is the shape factor of the upwelling radiance, and $\tilde{b}_b$ is the backscattering ratio b_b/b. Finally, $\Re$ is the same coefficient applied in M02 to account for the reflectance and refraction properties of the air-sea interface. The T18 code is available upon request to the authors.

2.4 RAMAN CORRECTION

Raman scattering can affect the water reflectance in clear waters, and it is entirely handled by the M02 method, which proved its importance compared to older f/Q LUT (Gentili and Morel, 1996). Instead, it is not considered in radiative transfer simulations underlying of P05 and L11 methods.

Aiming to introduce the approach adopted in this study for taking the Raman scattering into account, it is recalled that the BRDF correction coefficient is the ratio between modeled (circumflex accent) water reflectances:

$$C(\lambda,\Omega,\mathrm{IOP}) \equiv \frac{\hat{\rho}_w^{ex}(\lambda,\ \Omega_o,\mathrm{IOP})}{\hat{\rho}_w(\lambda,\Omega,\mathrm{IOP})}. \quad (13)$$

Eq. (2) is equivalent to Eq. (13), but here, the dependence on the atmospheric properties and the wind speed has been omitted to focus the discussion on the IOPs role as a *C* parameter.

The Raman scattering was not included in RT simulation for the QAA implementation. The fact that the Raman effect is "unknown" to QAA introduces a bias in the IOPs retrieval from the observed water reflectance (which naturally depends on Raman). For consistency, the IOPs must then be computed after removing the Raman effect from the observed water reflectance. Note that this consistency only refers to the $\rho_w \rightarrow$ IOPs relationship embedded in QAA. This approach is justified because Raman scattering can significantly affect the water reflectance spectrum but much less its directional dependence. The Raman component must be included in the RT model to account for its direct influence on the anisotropy of the water reflectance (*e.g.*, M02 method).

Different studies have been presented in the literature to model the Raman effect (Bartell et al., 1981; Lee et al., 2013; McKinna et al., 2016; Sathyendranath and Platt, 1998; Westberry et al.,

2013). For practical reasons, the present work refers to the Lee (2013) formulation. Precisely, the Raman effect is expressed as

$$R_{rs}(\lambda) = \frac{R_{rs}^{T}(\lambda)}{1 + RF(\lambda)} \tag{14}$$

where $R_{rs}^{T}(\lambda)$ and $R_{rs}(\lambda)$ indicate the remote sensing reflectance with and without the Raman contribution, respectively, and the $RF(\lambda)$ is

$$RF(\lambda) = \alpha(\lambda)\left(\frac{R_{rs}^{T}(440)}{R_{rs}^{T}(550)}\right) + \beta_1(\lambda)(R_{rs}^{T}(550))^{\beta_2(\lambda)}. \tag{15}$$

The approximation due to applying Eq. (15) with the R_{rs}^{T} value at the 560 nm band of OLCI is assumed to have a minor effect in terms of BRDF correction.

3 APPLICABILITY AND PERFORMANCE OF THE BRDF SCHEMES

3.1 BRDF PARAMETERIZATION IN TERMS OF OPTICAL REGIMES

The BRDF correction process depends on the retrieval of IOPs from $\rho_w(\lambda, \Omega)$, and to a lesser extent, from the atmospheric condition. The spectral properties are most relevant to relate $\rho_w(\lambda, \Omega)$ to IOPs through bio-optical algorithms. However, once IOPs have been computed, the spectral component disappears, and only the geometrical dependence remains (*i.e.*, apart from Raman scattering and fluorescence effects). This allows for a more general BRDF correction interpretation, as detailed below.

Input IOPs can be mapped into a new parameter space that allows a more direct understanding of the BRDF process without accounting for any spectral dependence. This concept, initially addressed by Morel et al. (2002) and then further elaborated by Mazeran (2017), is illustrated in Figure 1 based on the single scattering albedo

$$\tilde{\omega} = \frac{b}{a + b} \tag{16}$$

and the ratio of pure water to total backscattering

$$\eta_b = \frac{b_{bw}}{b_{bw} + b_{bp}}. \tag{17}$$

In this mapping, the IOPs appear only as a convenient intermediate to apply the BRDF correction. In other words, given an RTM and phase function, any $(\tilde{\omega}, \eta_b)$ model could represent the BRDF structure of the radiant field; for instance, the f/Q tables, generated through RTM, perfectly include this structure (assuming that the phase function is realistic); it is only the closure of $(\tilde{\omega}, \eta_b)$ with chlorophyll limiting it to Case-1 waters (Figure 1, right). The IOPs expression in terms of $(\tilde{\omega}, \eta_b)$ is hence viewed as a complementary way to explain results

obtained from BRDF-correction schemes, as well as to address performance comparisons through a common input parameter space. Note that this bi-dimensional view is only for a given phase function, which may depend on the IOPs (like in the M02 approach).

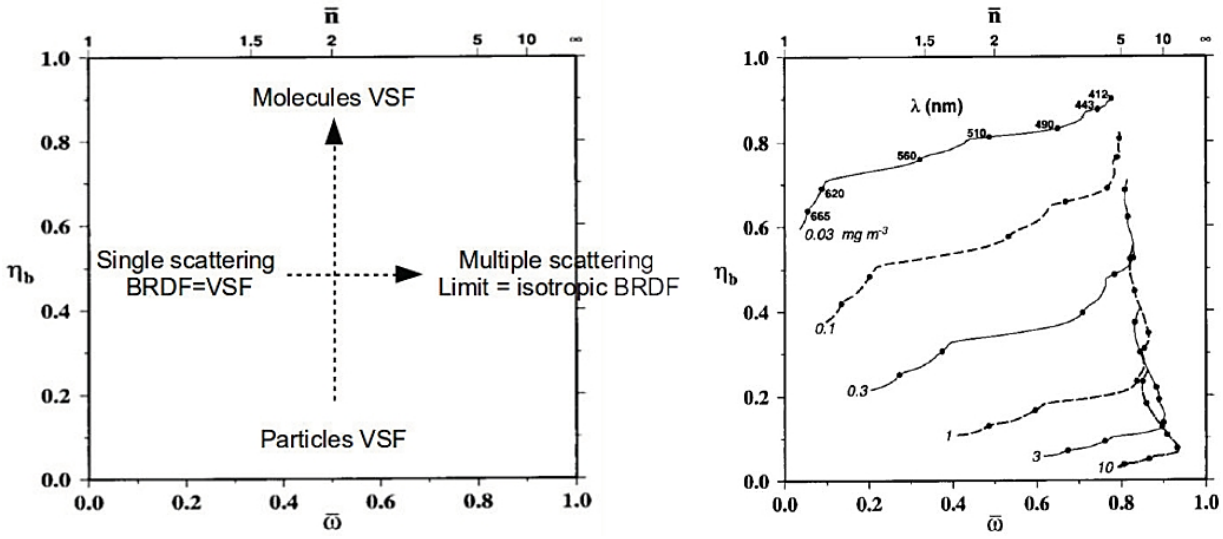

(a) (b)

Figure 1 Adapted from (Mazeran, 2017). (a) generic dependence of the BRDF on the particulate or water VSF in the ($\overline{\omega}$ and η_b) space, with limit cases overprinted; Background image from (Morel et al., 2002). (b) specific closure of $\overline{\omega}$ and η_b through chlorophyll (lines) and wavelength (dots on lines), as done in (Morel et al., 2002).

More specifically, the BRDF correction schemes can all be written as a function of (ω_b, η_b) where ω_b is the single *backscattering* albedo $\omega_b = \frac{b_b}{a+b_b}$. This is straightforward for PR05, with $\gamma_b = 1 - \eta_b$. For L11, we have $b_{bw}/(a+b_b) = \eta_b \omega_b$ and $b_{bp}/(a+b_b) = (1-\eta_b)\omega_b$. T18 has an explicit dependence on $\frac{b_b}{a} = \frac{\omega_b}{\omega_b - 1}$, what shows singularity for highly scattering waters (*i.e.*, when ω_b approaches 1). The same would be true with M02 if the full reflectance model $R_{rs} = \Re \frac{f}{Q} \frac{b_b}{a}$ were used; however, it is not the case as the $\frac{b_b}{a}$ term vanishes and is never computed for the BRDF correction.

For M02, the relationship between $\frac{f}{Q}(\lambda, Chl)$ and (ω_b, η_b) is more complex. It shall be understood that (λ, Chl) are only degrees of freedom used for the Case 1 parameterization, but the method inherently depends on (ω_b, η_b) through the radiative transfer simulations made during the f/Q tabulation. The product of $\frac{f}{Q}(\lambda, Chl)$ with $\frac{\omega_b(\lambda)}{\omega_b(\lambda)-1}$ only makes sense when an implicit link between (λ, Chl) and the IOP is satisfied through the Case 1 parameterization (which comes from Morel and Maritorena, 2001). On the contrary, reading the f/Q method with a Chl value not consistent with this internal constraint produces erroneous correction. As shown later, this formalism permits flagging the BRDF correction outside its domain of optical range.

3.2 BRDF CORRECTION APPLICABILITY

This section presents:

- the nominal range of validity of the BRDF correction schemes and
- the geometrical and spectral applicability of BRDF correction schemes with respect to selected polar-orbiting satellites and geostationary satellites.

Considered BRDF schemes are M02, P05, and L11. Features related to T18 are not reported because model revisions are in progress.

Table 2 Nominal range of validity of the BRDF correction schemes.

Parameter	M02	P05	L11
Spectral range	412.5–660 Morel et al. (2002) 350–700 nm LUT revision by B. Gentili	P05 LUTs do not explicitly depend on λ. Spectral limitations related to the simulated data to define the LUTs.	L11 LUTs do not explicitly depend on λ. Spectral limitations related to the simulated data to define the LUTs.
Seawater optical properties /Chl-a	Chl-a in the range [0.03-10] mg/m^3.	IOPs variability as defined in Park and Ruddick (2005).	IOPs variability as defined in the IOCCG dataset (IOCCG, 2006).
Applicable geometry / scattering angle	θ_s: 0°–75° θ_v: 0°–90° $\Delta\phi$: 0°–180°	θ_s: 0°-85° θ_v: 0°–87.5° $\Delta\phi$: 0°–180°	θ_s: 0°–75° θ_v:0°–70° $\Delta\phi$: 0°–180°
Cloud Cover	Clear sky	Cloud coverages 0-100% (at 5 m s^{-1} wind speed)	Clear sky
Wind speed	0–10 m s^{-1}	Wind speeds 0–10 m s^{-1} (cloud-free sky)	Simulations made with a wind speed of 5 m s^{-1}. In practice, its influence is neglected

3.2.1 Direct applicability

The direct applicability of the BRDF correction methods to different space missions is detailed for the measurement spectral intervals, the constraints due to the viewing and illumination geometry, as well as the cloud cover and the wind speed ranges (see Table 2 for details).

The P05 and L11 BRDF-correction schemes do not have an explicit wavelength dependence (see Eq. 7 and Eq. 8, respectively*; i.e.*, corresponding LUT are not indexed in terms of λ). Still, their validity is constrained by the range of Hydrolight simulations (and hence the variability of input IOPs) underlying the LUT implementations. This implicit constraint affects all BRDF correction schemes, as explained in Sec. 3.3.

3.2.2 Geometrical and spectral applicability of BRDF correction schemes

The geometrical and spectral application limits of BRDF correction schemes have been verified for polar orbiting and geostationary satellites. In addition to OLCI, the selected polar-orbiting sensor is the Ocean Color Instrument (OCI) sensor of the Plankton, Aerosol, Cloud, Ocean Ecosystem (PACE) mission of NASA.

Table 3 Geometrical and spectral applicability of BRDF correction schemes for selected polar-orbiting and geostationary satellites.

- (*) BRDF without an explicit dependence on **λ**, but applications are implicitly limited by the IOPs data set used to define BRDF LUTs (see Sec. 3.3).
- Spectral ranges are in nm.

				BRDF correction		
				M02	**P05**	**L11**
		Spectr		• 412.5–660 Morel et al. (2002) • 350–700 nm LUT revision by B. Gentili	• P05 LUTs do not explicitly depend on λ.	• L11 LUTs do not explicitly depend on λ.
		Geom		• θ_s: 0°–75° • θ_v: 0°–90° • $\Delta\phi$: 0°–180°	• θ_s: 0°-85° • θ_v: 0°–87.5° • $\Delta\phi$: 0°–180°	• θ_s: 0°–75° • θ_v:0°–70° • $\Delta\phi$: 0°–180°
Polar-orbiting satellites	**OLCI**	Spectr.	• 400 –1040	• $412.5 \leq \lambda \leq 660$ • $\lambda \leq$ 700 with LUT by B. Gentili.	• No explicit constraints (*)	• No explicit constraints (*)
		Geom.	• θ_S< 80° • θ_v< 55° • $\Delta\phi$ 0°-180°	• θ_s < 75° • θ_v full • $\Delta\phi$ full	• θ_s full • θ_v full • $\Delta\phi$ full	• θ_s < 75° • θ_v full • $\Delta\phi$ full
	PACE	Spectr.	• 340 –1040	• $412.5 \leq \lambda \leq 660$ • $350 \leq \lambda \leq 700$ with LUT by B. Gentili.	• No explicit constraints (*)	• No explicit constraints (*)
		Geom.	• θ_S< 75° • θ_v< 57° • $\Delta\phi$ 0°-180°	• θ_s full • θ_v full • $\Delta\phi$ full	• θ_v full • θ_s full • $\Delta\phi$ full	• θ_s full • θ_v full • $\Delta\phi$ full
Geostationary satellites	**GOCI**	Spectr.	• 412 –865	• $412.5 \leq \lambda \leq 660$ • $350 \leq \lambda \leq 700$ with LUT by B. Gentili.	• No explicit constraints (*)	• No explicit constraints (*)
	FCI	Spectr.	• 444 –1330	• $\lambda \leq 660$ • $\lambda \leq$ 700 with LUT by B. Gentili.	• No explicit constraints (*)	• No explicit constraints (*)
	3MI	Spectr.	• 410 –2130	• $412.5 \leq \lambda \leq 660$ • $350 \leq \lambda \leq 700$ with LUT by B. Gentili.	• No explicit constraints (*)	• No explicit constraints (*)
	MET image	Spectr.	• 443 –13345	• $\lambda \leq 660$ • $\lambda \leq$ 700 with LUT by B. Gentili.	• No explicit constraints (*)	• No explicit constraints (*)
	All	Geom.	• θ_S< 80° • θ_v< 70° • $\Delta\phi$ 0°-180°	• θ_s < 75° • θ_v full • $\Delta\phi$ full	• θ_s full • θ_v full • $\Delta\phi$ full	• θ_s < 75° • θ_s full • $\Delta\phi$ full

Considered geostationary satellites include the Geostationary Ocean Color Imager operated by Korea Ocean Satellite Center (GOCI, see also Figure 2 and details reported by Lee et al. (2015)), as well as the following satellite operated by EUMETSAT: 1) the MTG Flexible Combined Imager (FCI), 2) the EPS-SG Multi-Viewing Multi-Channel Multi-Polarisation Imaging (3MI) satellite, and 3) the METimage. Wavelength interval and ranges of viewing zenith angle, sun zenith angle, and

relative azimuth angle of each BRDF correction scheme are reported in Table 3 for direct comparison with those of the space sensors

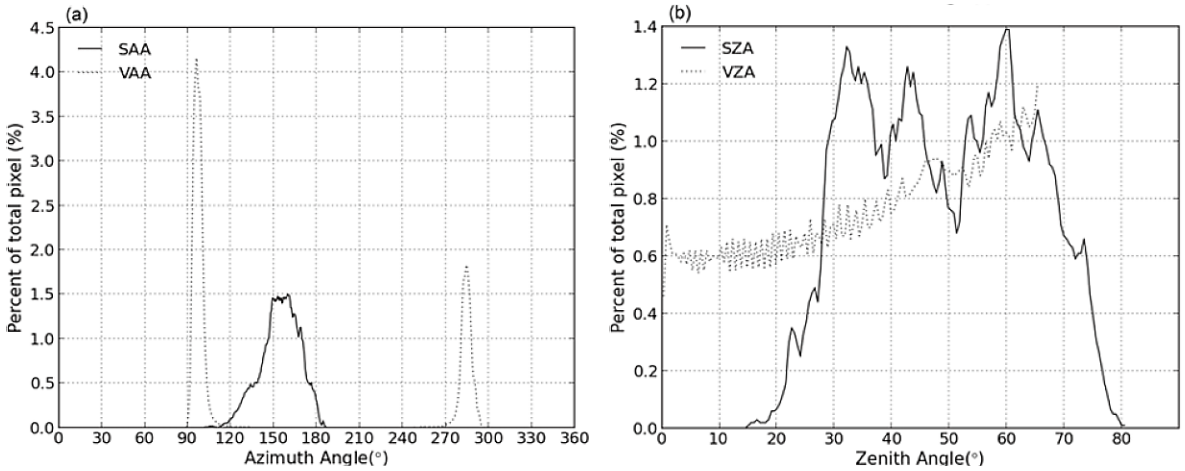

Figure 2 GOCI features reproduced from Lee et al. (2015) considered in this study as a test case: "Diagram of the angular distribution (a: azimuth angle, b: zenith angle) in which the different lines denote geometry (solid: solar azimuth and zenith, dotted: viewing azimuth and zenith) within the study area."

3.3 BRDF OPTICAL RANGES AND FLAGGING

All BRDF methods are based on radiative transfer simulations (even T18 in some components). Hence, their validity depends on the range of IOPs used during their implementation. It is remarked that the validity range can be expressed in the (ω_b, η_b) plane and is illustrated for M02, P05, and L11 in Figure 3 (black dots) on both linear and logarithmic scales for the ω_b axis. For M02, this corresponds to the Morel and Maritorena (2001) bio-optical models applied to the range of wavelengths and chlorophyll concentration of the LUTs. Values for P05 are given by the IOP model described in Park and Ruddick (2005). Values used by L11 come from the IOCCG dataset (IOCCG, 2006).

The number of training points varies significantly among the methods. A smaller number of points is used in M02. However, since this BRDF correction relies entirely on a single LUT indexed by wavelength, its potential limitation only refers to interpolation error. The number of points is more crucial for P05 and L11 because it impacts the relationships between reflectance and (ω_b, η_b) derived by numerical fitting. In this respect, the 500 simulations of the IOCCG dataset used by L11 give the denser data set.

The most critical aspect resides in the coverage of each method in the scattering regime. M02 is very limited in terms of ω_b (below 0.2), likely because the scattering particles covarying with phytoplankton in the Case-1 model also absorb light, whereas the sediments involved in P05 and L11 scatter more than they absorb. The logarithmic scale shows that M02 is also more limited for the minimal value of ω_b, which again can be explained by the absence of a purely absorbing component (CDOM) in the Case-1 assumptions. P05 is the only method containing points at $\eta_b = 1$, *i.e.*, $b_{bp} = 0$ but for different values of absorption hence different values of ω_b.

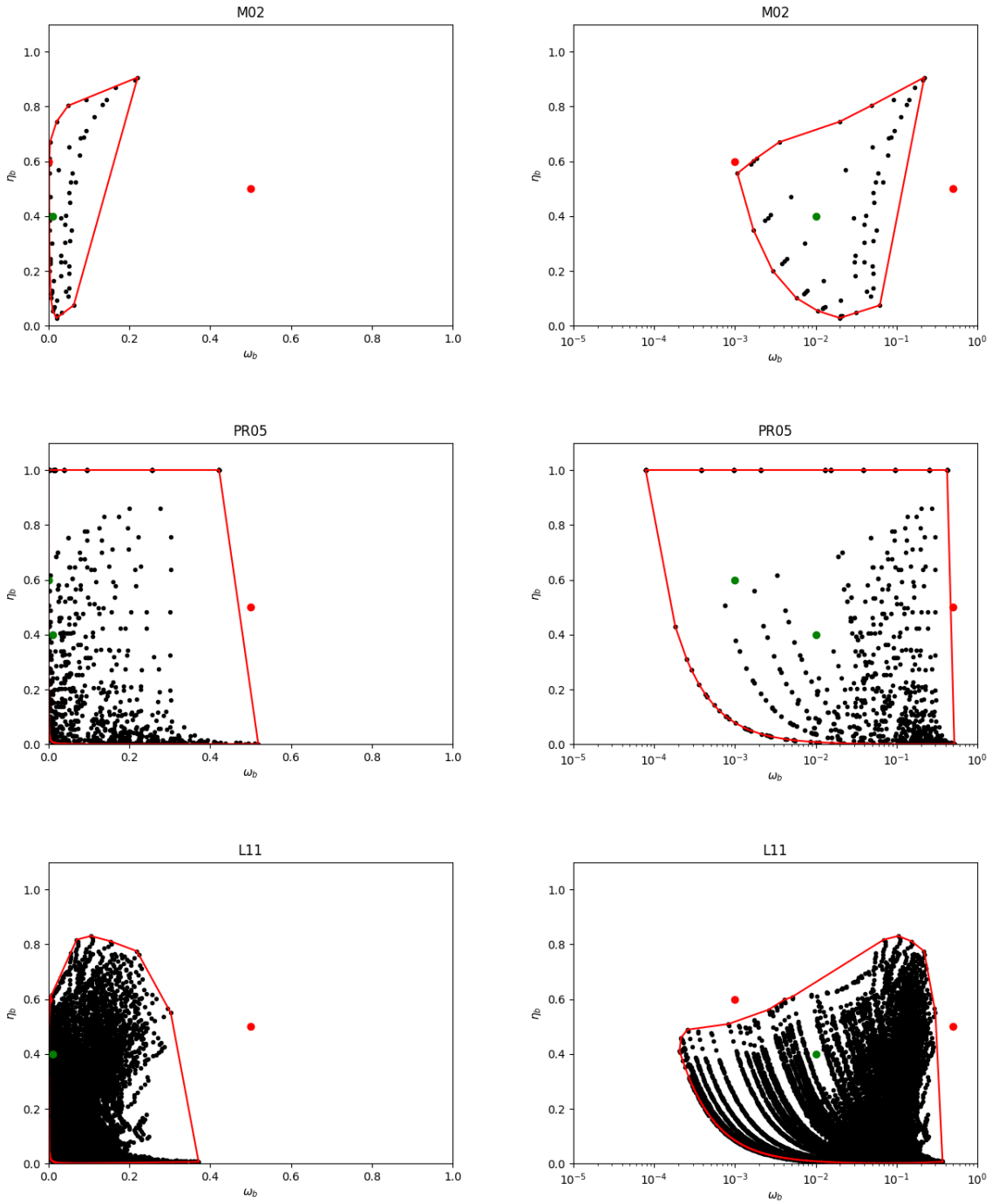

Figure 3 Domain of validity of M02, P05 and L11 schemes (from top to bottom) in the (ω_b, η_b) space, left with ω_b in linear scale, right with ω_b in logarithmic scale. Black dots correspond to the simulated data used in the derivation of each scheme. The red curve is the envelope of this data set. The three colored dots are examples of (ω_b, η_b) values, in green if within the valid range, in red if outside.

The study considers that the validity domain of each method is given by the envelope containing the training points (red curve in Figure 3). The points defining this envelope are computed by the convex hull algorithm (available in Python Scipy package). Roughly, the domains of the considered methods are ordered (*i.e.,* included) as:

$$M02 \subset L11 \subset P05$$

It is then possible to identify whether a given set of IOPs, *i.e.*, a point (ω_b, η_b), resides inside or outside the convex envelope. For this, the nodes $N^i = (\omega_b^i, \eta_b^i)$ of the convex hull are stored in the (ω_b, η_b) vector space in an ordered manner (lexicographically, from neighbor to neighbor).

Any point $P = (\omega_b, \eta_b)$ is inside the domain *if and only if* all vector products $\overrightarrow{PN^i} \wedge \overrightarrow{PN^{i+1}}$ are positive for all nodes, *i.e.*:

$$(\omega_b^i - \omega_b) * (\eta_b^{i+1} - \eta_b) - (\omega_b^{i+1} - \omega_b) * (\eta_b^i - \eta_b) > 0 \quad \forall\, i \tag{18}$$

A new flag OUT_OF_RANGE_BRDF is defined accordingly in the OLCI processor. Three examples of (ω_b, η_b) data points are plotted in Figure 3, sometimes falling inside (in green) or outside (in red) the domain of each method. The extent of the validity domain is crucial to the BRDF performance. However, note that the VSF should complete this 2D view on any point of the domain. For instance, L11 presents a broader domain than M02, but its unique particle VSF may be more limited than the more evolved VSF of M02, varying with chlorophyll concentration.

3.4 SUMMARY OF BRDF CORRECTION ASSESSMENTS AND RECOMMENDATIONS

The study has verified the performance of M02, P05, and L11 BRDF correction schemes as detailed in the PVR. The assessment is based on field measurements, matchup data, and comparisons between Sentinel A and B image processing results. A summary of the assessments and the rationale for selecting the L11 method for the operational BRDF correction of OLCI data are presented next (see also Table 4).

Table 4 Summary of BRDF assessment results.

	No BRDF	M02	P05	L11
Field measurements	Third option	Second option	Second option	Best option
Matchup data	Best option	Third option	Second option	Second option
OLCI-A and B images	Third option	Second option	Second option	Best option

The evaluation of the BRDF correction based on in situ data relied on measurements performed with the Optical Floating System (OFS, Talone et al., 2018) in the Mediterranean and Black Sea, as well as measurements performed with two TriOS RAMSES systems at the NIOZ Jetty Station (NJS) the Dutch Wadden Sea. For both datasets, L11 was the BRDF correction scheme with better performance for most cases.

The evaluation based on the reference dataset provided by EUMETSAT was used to compare BRDF correction factors computed from satellite data and analyze matchup results. Results exclusively based on satellite data showed similar L11 and P05 behaviors across the optical water types of the AERONET-OC sites. However, the BRDF corrected reflectances retrieved with the P05

scheme were consistently higher than L11 by a few percent. The matchup results have shown that the P05 and L11 BRDF correction schemes had the best performance at the MOBY site. The L11 method yielded better scores among the tested BRDF corrections at 443, 490 and/or 560 nm for the AERONET-OC sites. Considering all input data files provided by EUMETSAT, the best agreement between in situ and OLCI measurements was obtained without applying any BRDF correction, although the L11 was the best performer of the BRDF schemes.

The analysis of OLCI-A and B images has shown the need for carefully selecting test images due to the possible presence of anomalous cases. Upon this screening, the assessment of the BRDF correction based on different viewing geometries showed that the L11 model gives better results among the tested approaches (*i.e.*, without BRDF correction or applying the M02 and P05 models).

Based on all the above findings, the L11 BRDF scheme was more successful in reducing geometric impacts. The study recommendation is to rely on L11 BRDF correction implementation in the IPF for the operational processing of OLCI data. However, access to OLCI data that are not BRDF corrected should be explored, for instance, as a users' post-processing option. The rationale is that some performance metrics are still inconclusive due to the analysis design. The main limiting factors are:

- The use of 15 AERONET-OC input files, of which only 3 for S3B.
- The data distribution in the AERONET-OC input files skewed toward complex waters due to the nature and location of the 12 AERONET-OC sites.
- The matchup in situ dataset provided by EUMETSAT was BRDF corrected with the M02 method.
- The assumption of a *stable atmosphere* and *the same atmospheric correction* in the comparison and analyses for different satellite viewing geometries.
- Further confounding effects such as camera biases, residuals in the SVC, aerosol detection errors, and natural variability within the timeframe of the comparison.

4 BRDF CORRECTION UNCERTAINTY

This section addresses the evaluation of the uncertainty associated with the BRDF correction. Specifics topics are:

- problem statement,
- implementation of the proposed solution, and
- results.

4.1 PROBLEM STATEMENT

Measurement uncertainty is a non-negative parameter characterizing the dispersion of the individual measures being attributed to a measurand (the BRDF correction, in this case). The measurement uncertainty comprises various components: some may be evaluated from the statistical distribution of a series of measurements and can be characterized as standard

deviation (type A). Others may be evaluated from probability density functions based on experience or additional information sources (type B; JCGM, 2008).

Examples of type A evaluation of the uncertainty of the BRDF correction have been proposed in the literature (Talone et al., 2018). Results are specific to the environmental condition of the experiment (*e.g.*, IOPs, sun zenith, sea state, cloud coverage), which implicitly (as IOPs, sun zenith) or explicitly (as environmental variability) contribute to uncertainty estimate. Note that determining the BRDF accuracy in any optical regimes of operational interest would require corresponding reference measurements. Although this ideal condition cannot be fulfilled in practice, the collection of additional in situ data must be prioritized to validate BRDF correction results and related uncertainties.

Alternative to type-A evaluation, numerical simulations (type-B) can be applied to estimate the BRDF correction uncertainty. Note that the validity of BRDF accuracy estimates through numerical simulation depends on 1) the underlying model accuracy (*e.g.*, due to discretization, numerical solutions), 2) assumptions (*e.g.*, phase function, unless it is applied as an independent parameter or LUT dimension), and 3) approximations (*e.g.*, LUTs regression).

Aware that an indicator of the expected BRDF correction performance is of primary importance for the users' community, the approach followed by this study is:

- performing a replicability analysis of the BRDF correction across different methods, and
- formulating on this basis an objective pixel-based quality control/assurance index.

4.2 REPLICABILITY ANALYSIS

A replicability analysis has been applied to the BRDF correction, including M02, P05, and L11. The replicability index (r) has been computed as the standard deviation of the BRDF corrections obtained with the models mentioned above, relying on the CoastColour IOPs dataset (Nechad et al., 2015) and for the following geometries $\theta_s = (0{,}75)$; $\theta_v = (0{,}75)$; and $\Delta\phi = (0{,}180)$, *i.e.*:

$$r(\theta_s, \theta_v, \Delta\phi, \mathrm{IOP}) = std(C_{M02}(\theta_s, \theta_v, \Delta\phi, \mathrm{IOP}), C_{P05}(\theta_s, \theta_v, \Delta\phi, \mathrm{IOP}), C_{L11}(\theta_s, \theta_v, \Delta\phi, IOP)). \quad (19)$$

Justified by the relatively minor dependence of the random component of the BRDF uncertainty on the IOPs (Talone et al., 2018), r coefficients have been averaged over the IOP dimension, leading to the definition of the $\bar{r}(\theta_s, \theta_v, \Delta\phi)$.

4.3 RESULTS

Results in absolute terms (*i.e.*, in the same units of C) are shown in Figure 4 as polar plots corresponding to a specific θ_s , namely 0°, 15°, 30°, 45°, 60°, and 75°, and the radial and angular dimensions representing θ_v and $\Delta\phi$, respectively.

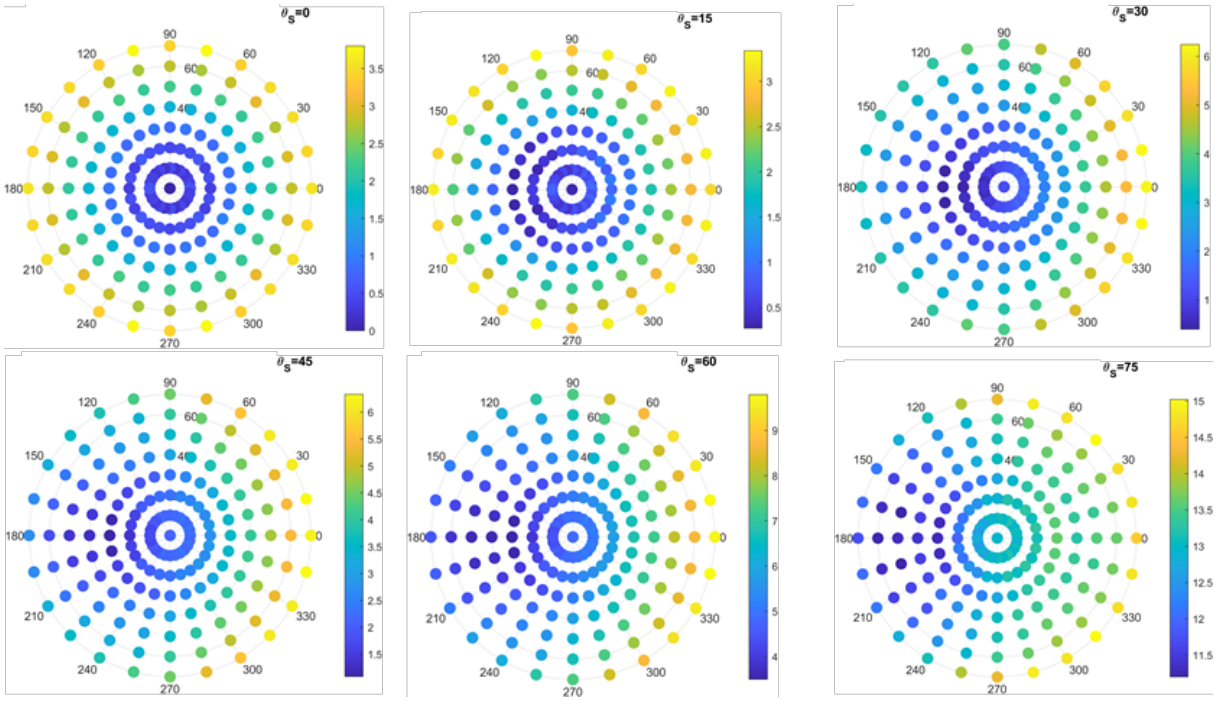

Figure 4 Polar plots of the replicability index for θ_s= 0°, 15°, 30°, 45°, 60°, and 75°. Radial and angular dimensions represent θ_v and $\Delta\phi$, respectively. Lower values of the replicability index are associated with lower (type-A) uncertainties.

The same values are summarized in Figure 5, where the replicability indices are displayed only as a function of θ_s jointly with the corresponding polynomial fit overplotted for convenience.

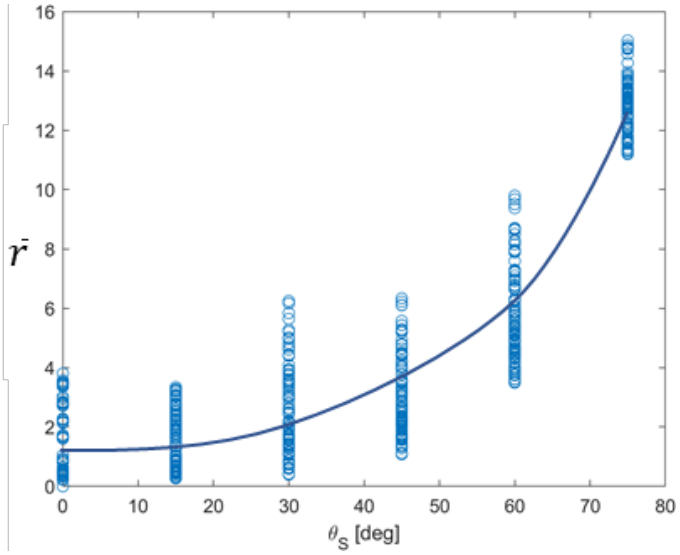

Figure 5 Replicability index as a function of θ_s. The blue line is a polinomial fit of $\bar{r}$. Different data points (hollow blue circles) at fixed θ_s correspond to different viewing geometries (θ_s and $\Delta\phi$).

5 IMPLEMENTATION OF THE BRDF MODULE

This section refers to the software implementation of the BRDF module and its operational applications. Considered topics include:

- conventions and data flow, and
- the architecture of the BRDF module within the IPF.

5.1 CONVENTIONS AND DATA FLOW

The zenith and azimuth angles definition follow the OLCI convention detailed in Figure 6.

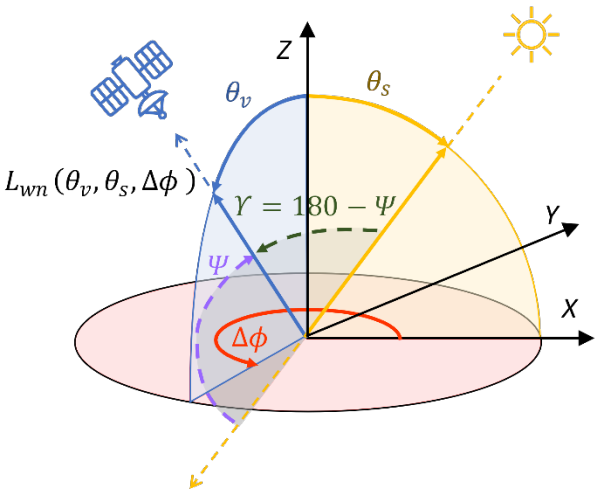

Figure 6 The OLCI convention is applied in this document to define the viewing zenith angle and the relative azimuth angle.

The BRDF correction process starts with the spectral observation ρ_w to retrieve IOPs. The forward BRDF model uses these IOPs to compute the water reflectances $\hat{\rho}_w$ and $\hat{\rho}_w^{ex}$, respectively in the observation geometry and the normalized geometry. The BRDF correction coefficient is computed as $C = \hat{\rho}_w^{ex}/\hat{\rho}_w$, and the exact water reflectance as $\rho_w^{ex} = C\rho_w$.

5.2 THE ARCHITECTURE OF THE BRDF MODULE

The code accounts for two main elements:

- the core module for what relates to the strict BRDF function plugged into the IPF. This core module is developed in the C/C++ programming language as a self-consistent computing framework and
- the wrapper in Python/cython to call the core module outside the IPF.

This architecture foresees two main use-cases (see Figure 7) to operate inside or outside the IPF.

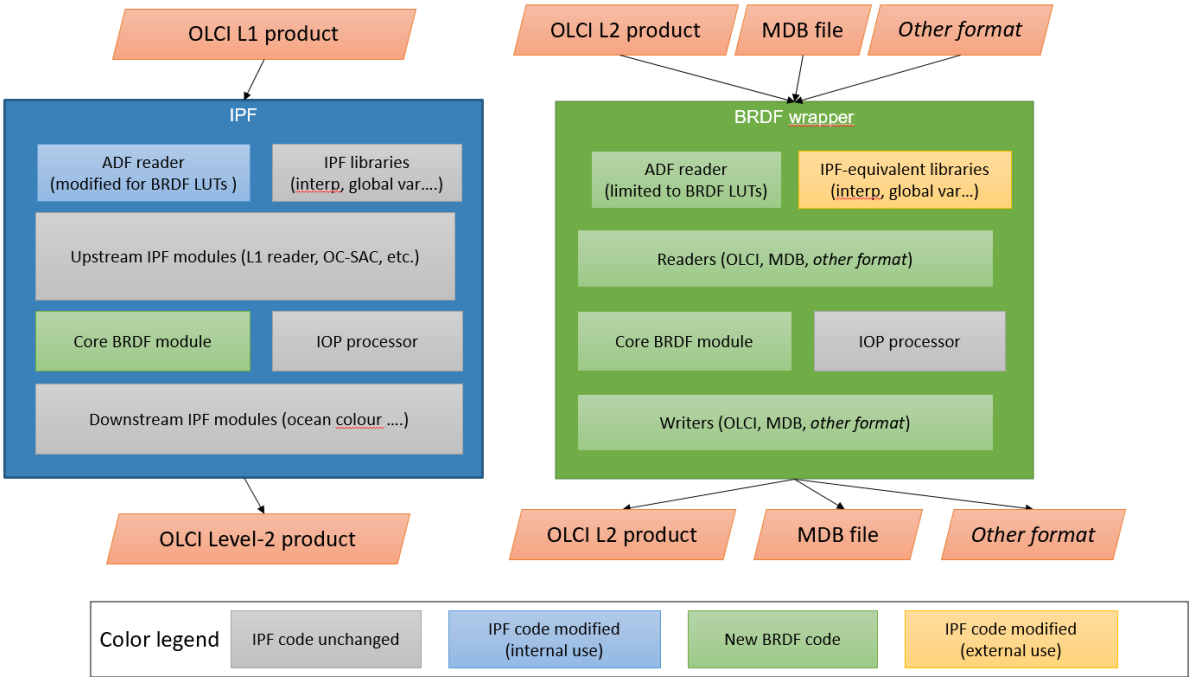

Figure 7 BRDF architecture use-cases in the IPF (left) and with a wrapper (right).

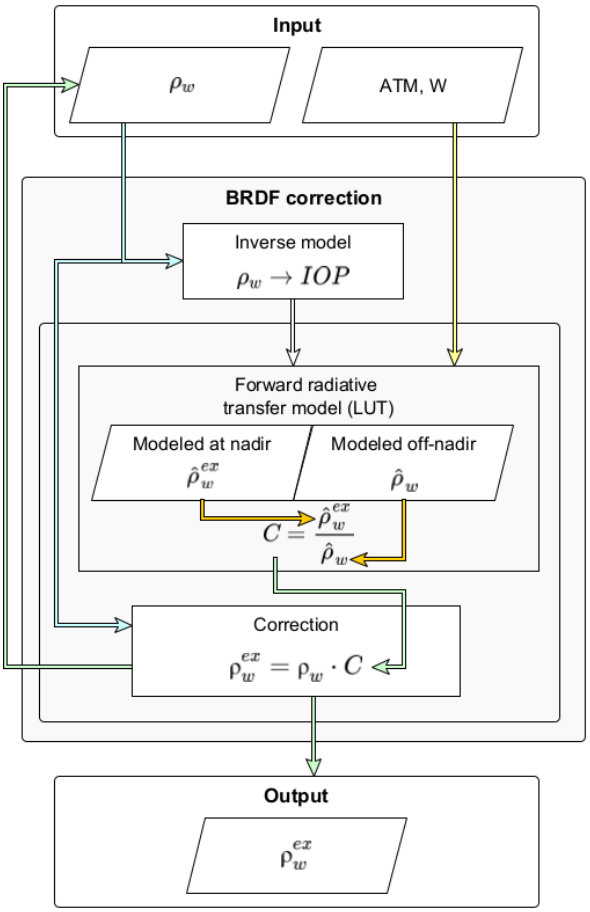

Figure 8 Data flow of the core BRDF module

5.2.1 Auxiliary Data Files

The ADF of the Level-2 IPF ("OCP" file) includes all LUTs and auxiliary data. Each method is distinguished into a dedicated group (*e.g.*, M02, P05, etc.). Importantly, angles follow the OLCI convention described above (Figure 6). The validity range is stored by the envelope of the training points used by each method in the (ω_b, η_b) space, as described in section 3.3.

5.2.2 Setup within the Instrument Processing Facility

The BRDF module operates inside the IPF on a given pixel (*pix_t* data structure). Computing tasks are executed by nested sub-components, which can be called iteratively, as shown in Figure 8.

5.2.3 Testing framework

The forward component of each BRDF module implementation in the IPF has been tested with simulated data and independent implementations of the BRDF correction scheme by team members.

6 GUIDELINES FOR FUTURE DEVELOPMENTS

Studies on BRDF correction developments have been conducted for two decades, yet the ocean color community recognizes the need for improvements. The underlying difficulty is that the BRDF correction cannot be expressed as an exact radiative transfer solution applicable to a remote sensing image on a pixel basis. Instead, it is necessary to rely on approximations as an optimal trade-off between accuracy requirements and operational constraints.

The present work has analyzed state-of-the-art BRDF correction schemes presented in the literature to find the one most suitable for processing OLCI data. Findings have also allowed defining the following guidelines for future BRDF correction developments:

- work plan to express the BRDF uncertainty budget as a function of input water reflectances, and
- design of a new BRDF correction model building on the strengths of all tested approaches.

6.1 ENHANCED DEFINITION OF THE BRDF CORRECTION UNCERTAINTY

A strict estimation of the uncertainty affecting the BRDF correction would require the availability of an extensive dataset of in situ measurements at varying geometries and IOPs. Since this is not feasible, the study has presented a pixel-based index for the quality control/assurance of radiometric products. A proxy of the BRDF correction uncertainty has also been designed based on the repeatability analysis of the tested BRDF correction results.

Additional developments need to consider a genuine uncertainty propagation from the input water reflectance into the retrieved IOPs and, finally, into the BRDF correction results. A preliminary analysis starting from the IOPs uncertainty was performed in this study. Results indicate that only a minor part of the uncertainty of the estimated IOPs is transferred to the BRDF correction (10-30% spectrally variable and depending on the correction model).

A plan to create the uncertainties LUT has been discussed with the UK National Physical Laboratory (NPL). The foreseen scheme for uncertainty propagation from water reflectance into

IOPs, then into BRDF correction coefficients, and again into water reflectances is to rely on Monte Carlo simulations. A direct approach is possible for in situ measurements but not for satellite images due to computing constraints. For this latter case, the solution is to rely on MC-derived LUT of uncertainty. Results obtained with the uncertainty LUT could complement those of the repeatability study (summed in quadrature, *i.e.*, assuming no covariance of these sources).

6.2 NEW DESIGN OF THE BRDF CORRECTION MODEL

The assessments based on in situ and satellite data have led this study to recommend the L11 method for OLCI data processing. Indeed, L11 and P05 have similar results, but the former showed a better performance. Notable L11 features are:

1. applicable in both Case 1 and 2 waters,
2. IOP-centered,
3. analytically invertible
4. in principle, reversible and convertible to any other geometry

However, factors limiting the L11 performance are:

1. the Raman effect is excluded,
2. the Petzold scattering phase function (Petzold, 1972) is used for all particles, which is contrary at least to experimental evidence in *Chl*-dominated waters, and
3. the variability range of IOPs for the LUT creation with Hydrolight is limited.

Accounting for the difficulty of relying on an analytical formulation such as T18, the following guidelines are recommended to develop a new BRDF correction by gathering favorable characteristics from the tested approaches:

1. adopt the L11 main design,
2. use Fournier-Forand scattering phase functions (Fournier, 2007; Fournier and Forand, 1994) for both phytoplankton and non-algal scattering,
3. extend the IOPs variability in comparison to L11 (Lee et al., 2002, 2011), for instance, by referring to the Coastcolour data (Nechad et al., 2015) ,
4. revise the empirical steps of the QAA to retrieve the IOPs from the water reflectance and provide a performance assessment,
5. account for Raman scattering (but also verify the performance when Raman is excluded), and
6. complement BRDF correction results with the accuracy estimates.

REFERENCES

Bartell, F.O., Dereniak, E.L., Wolfe, W.L., 1981. The Theory And Measurement Of Bidirectional Reflectance Distribution Function (Brdf) And Bidirectional Transmittance Distribution Function (BTDF), in: Hunt, G.H. (Ed.), Radiation Scattering in Optical Systems. Presented at the 1980 Huntsville Technical Symposium, Huntsville, United States, pp. 154–160. https://doi.org/10.1117/12.959611

Bricaud, A., Morel, A., Babin, M., Allali, K., Claustre, H., 1998. Variations of light absorption by suspended particles with chlorophyll *a* concentration in oceanic (case 1) waters: Analysis

and implications for bio-optical models. J. Geophys. Res. Oceans 103, 31033–31044. https://doi.org/10.1029/98JC02712

Ciotti, Á.M., Lewis, M.R., Cullen, J.J., 2002. Assessment of the relationships between dominant cell size in natural phytoplankton communities and the spectral shape of the absorption coefficient. Limnol. Oceanogr. 47, 404–417. https://doi.org/10.4319/lo.2002.47.2.0404

EUMETSAT, 2021. Sentinel-3 OLCI Marine User Handbook, version 1H, Technical report. Ref. EUM/OPS-SEN3/MAN/17/907205.

Fournier, G.R., 2007. Backscatter corrected Fournier-Forand phase function for remote sensing and underwater imaging performance evaluation, in: Levin, I.M., Gilbert, G.D., Haltrin, V.I., Trees, C.C. (Eds.), Current Research on Remote Sensing, Laser Probing, and Imagery in Natural Waters. Presented at the SPIE Proceedings, Moscow, Russian Federation, pp. 66150N-66150N–7. https://doi.org/10.1117/12.740463

Fournier, G.R., Forand, J.L., 1994. Analytic Phase Function for Ocean Water, in: Ocean Optics XII. SPIE, pp. 194–201. https://doi.org/10.1117/12.190063

Gordon, H.R., Clark, D.K., 1981. Clear water radiances for atmospheric correction of coastal zone color scanner imagery. Appl. Opt. 20, 4175. https://doi.org/10.1364/AO.20.004175

Gregg, W.W., Carder, K.L., 1990. A simple spectral solar irradiance model for cloudless maritime atmospheres. Limnol. Oceanogr. 35, 1657–1675. https://doi.org/10.4319/lo.1990.35.8.1657

Haltrin, V.I., Lee, M.E., Shybanov, E.B., Arnone, R.A., Weidemann, A.D., Mankovsky, V.I., Pegau, W.S., Ladne, S.D., 2002. Relationship between backscattering and beam scattering coefficients derived from new measurements of light scattering phase functions. Presented at the Ocean Optics XVI, Santa Fe, New Mexico, USA., p. 6. Ocean Optics XVI. Santa Fe, New Mexico, USA.

He, S., Zhang, X., Xiong, Y., Gray, D., 2017. A Bidirectional Subsurface Remote Sensing Reflectance Model Explicitly Accounting for Particle Backscattering Shapes. J. Geophys. Res. Oceans 122, 8614–8626. https://doi.org/10.1002/2017JC013313

JCGM, 2008. Evaluation of measurement data — Guide to the expression of uncertainty in measurement.

Lee, C.S., Yeom, J.M., Lee, H.L., Kim, J.-J., Han, K.-S., 2015. Sensitivity analysis of 6S-based look-up table for surface reflectance retrieval. Asia-Pac. J. Atmospheric Sci. 51, 91–101. https://doi.org/10.1007/s13143-015-0062-9

Lee, Z., Carder, K.L., Arnone, R.A., 2002. Deriving inherent optical properties from water color: a multiband quasi-analytical algorithm for optically deep waters. Appl. Opt. 41, 5755. https://doi.org/10.1364/AO.41.005755

Lee, Z., Hu, C., Shang, S., Du, K., Lewis, M., Arnone, R., Brewin, R., 2013. Penetration of UV-visible solar radiation in the global oceans: Insights from ocean color remote sensing. J. Geophys. Res. Oceans 118, 4241–4255. https://doi.org/10.1002/jgrc.20308

Lee, Z.P., Du, K., Voss, K.J., Zibordi, G., Lubac, B., Arnone, R., Weidemann, A., 2011. An inherent-optical-property-centered approach to correct the angular effects in water-leaving radiance. Appl. Opt. 50, 3155. https://doi.org/10.1364/AO.50.003155

Loisel, H., Morel, A., 1998. Light scattering and chlorophyll concentration in case 1 waters: A reexamination. Limnol. Oceanogr. 43, 847–858. https://doi.org/10.4319/lo.1998.43.5.0847

Mazeran, C., 2017. BRDF correction over Case-2 waters. SOLVO report to ESA, ref. SOLVO/TVU/16/IDE/D8 (accessible on demand).

McKinna, L.I.W., Werdell, P.J., Proctor, C.W., 2016. Implementation of an analytical Raman scattering correction for satellite ocean-color processing. Opt. Express 24, A1123. https://doi.org/10.1364/OE.24.0A1123

Mobley, C.D., 1994. Light and Water. Radiative Transfer in Natural Waters. Academic Press.

Mobley, C.D., Boss, E., Roesler, C.S., 2021. Ocean Optics Web Book [WWW Document]. URL https://www.oceanopticsbook.info/

Mobley, C.D., Werdell, J., Franz, B., Ziauddin Ahmad, Bailey, S., 2016. Atmospheric Correction for Satellite Ocean Color Radiometry. NASATM-2016-217551. https://doi.org/10.13140/RG.2.2.23016.78081

Morel, A., 1974. Optical Properties of Pure Seawater, in: Aspects of Oceanography, N. G. Jerlov and E. Steemann Nielsen (Eds.) Chap. 1. Academic Press Inc., New York, pp. 1–24.

Morel, A., Antoine, D., Gentili, B., 2002. Bidirectional reflectance of oceanic waters: accounting for Raman emission and varying particle scattering phase function. Appl. Opt. 41, 6289. https://doi.org/10.1364/AO.41.006289

Morel, A., Gentili, B., 1996. Diffuse reflectance of oceanic waters III Implication of bidirectionality for the remote-sensing problem. Appl. Opt. 35, 4850. https://doi.org/10.1364/AO.35.004850

Morel, A., Gentili, B., 1993. Diffuse reflectance of oceanic waters II Bidirectional aspects. Appl. Opt. 32, 6864. https://doi.org/10.1364/AO.32.006864

Morel, A., Maritorena, S., 2001. Bio-optical properties of oceanic waters: A reappraisal. J. Geophys. Res. Oceans 106, 7163–7180. https://doi.org/10.1029/2000JC000319

Nechad, B., Ruddick, K., Schroeder, T., Oubelkheir, K., Blondeau-Patissier, D., Cherukuru, N., Brando, V., Dekker, A., Clementson, L., Banks, A.C., Maritorena, S., Werdell, P.J., Sá, C., Brotas, V., Caballero de Frutos, I., Ahn, Y.-H., Salama, S., Tilstone, G., Martinez-Vicente, V., Foley, D., McKibben, M., Nahorniak, J., Peterson, T., Siliò-Calzada, A., Röttgers, R., Lee, Z., Peters, M., Brockmann, C., 2015. CoastColour Round Robin data sets: a database to evaluate the performance of algorithms for the retrieval of water quality parameters in coastal waters. Earth Syst. Sci. Data 7, 319–348. https://doi.org/10.5194/essd-7-319-2015

Park, Y.-J., Ruddick, K., 2005. Model of remote-sensing reflectance including bidirectional effects for case 1 and case 2 waters. Appl. Opt. 44, 1236–1249. https://doi.org/10.1364/AO.44.001236

Petzold, T.J., 1972. Volume Scattering Functions for Selected Ocean Waters (Technical Report), SIO. Scripps Institution of Oceanography.

Pope, R.M., Fry, E.S., 1997. Absorptium Spectrum (380-700 nm) of Pure Water: II. Integrating Cavity Measurements. Appl Opt. 36, 8710–8723.

Remote Sensing of Inherent Optical Properties: Fundamentals, Tests of Algorithms, and Applications., 2006. . International Ocean Colour Coordinating Group (IOCCG).

Roesler, C.S., Perry, M.J., 1995. In situ phytoplankton absorption, fluorescence emission, and particulate backscattering spectra determined from reflectance. J. Geophys. Res. 100, 13279. https://doi.org/10.1029/95JC00455

Sathyendranath, S., Platt, T., 1998. Ocean-color model incorporating transspectral processes. Appl. Opt. 37, 2216. https://doi.org/10.1364/AO.37.002216

Smith, R.C., Baker, K.S., 1981. Optical properties of the clearest natural waters (200–800 nm). Appl. Opt. 20, 177. https://doi.org/10.1364/AO.20.000177

Steinmetz, F., 2021. Spectral matching Atmospheric Correction for Sentinel Ocean colour measurements (SACSO) [WWW Document]. URL https://www.eumetsat.int/SACSO

Sullivan, J.M., Twardowski, M.S., 2009. Angular shape of the oceanic particulate volume scattering function in the backward direction. Appl. Opt. 48, 6811. https://doi.org/10.1364/AO.48.006811

Talone, M., Zibordi, G., Lee, Z., 2018. Correction for the non-nadir viewing geometry of AERONET-OC above water radiometry data: an estimate of uncertainties. Opt. Express 26, A541. https://doi.org/10.1364/OE.26.00A541

Twardowski, M., Tonizzo, A., 2018. Ocean Color Analytical Model Explicitly Dependent on the Volume Scattering Function. Appl. Sci. 8, 2684. https://doi.org/10.3390/app8122684

Twardowski, M.S., Boss, E., Macdonald, J.B., Pegau, W.S., Barnard, A.H., Zaneveld, J.R.V., 2001. A model for estimating bulk refractive index from the optical backscattering ratio and the implications for understanding particle composition in case I and case II waters. J. Geophys. Res. Oceans 106, 14129–14142. https://doi.org/10.1029/2000JC000404

Twardowski, M.S., Boss, E., Sullivan, J.M., Donaghay, P.L., 2004. Modeling the spectral shape of absorption by chromophoric dissolved organic matter. Mar. Chem. 89, 69–88. https://doi.org/10.1016/j.marchem.2004.02.008

Ulloa, O., Sathyendranath, S., Platt, T., 1994. Effect of the particle-size distribution on the backscattering ratio in seawater. Appl. Opt. 33, 7070. https://doi.org/10.1364/AO.33.007070

Westberry, T.K., Boss, E., Lee, Z., 2013. Influence of Raman scattering on ocean color inversion models. Appl. Opt. 52, 5552. https://doi.org/10.1364/AO.52.005552

Zaneveld, J.R.V., 1995. A theoretical derivation of the dependence of the remotely sensed reflectance of the ocean on the inherent optical properties. J. Geophys. Res. 100, 13135. https://doi.org/10.1029/95JC00453

Zhang, X., Hu, L., He, M.-X., 2009. Scattering by pure seawater: Effect of salinity. Opt. Express 17, 5698. https://doi.org/10.1364/OE.17.005698

Zibordi, G., Donlon, C.J., Parr, A.C., 2014. Optical radiometry for ocean climate measurements, Experimental methods in the physical sciences. Academic Press, Waltham, MA.

APPENDIX

A. DEFINITION OF RADIOMETRIC QUANTITIES

Radiometric quantities are defined following the notation adopted by the SoW and the reference documents (EUMETSAT, 2021). It is however noted that slightly different formalism can be found in the literature (for additional details, see Mobley et al., 2016; Zibordi et al., 2014).

A.1. Water-leaving radiance

The water-leaving radiance is the spectral radiant flux emerging from the sea surface at a given direction per unit solid angle and unit projected area. It is denoted as $L_{\mathrm{w}}(\lambda, \theta_{\mathrm{v}}, \theta_S, \Delta\phi)$, where λ is the measurement central wavelength, θ_{v} the viewing zenith angle, θ_S the sun zenith angle, and $\Delta\phi$ the relative azimuth angle between the measurement direction and the sun. The compact notation $\Omega = (\theta_v, \theta_S, \Delta\phi)$, particularly $\Omega_{\mathrm{o}} = (0, 0, 0)$ to indicate the fully normalized geometry with nadir view and sun at zenith, can also be employed in this document to indicate the viewing and illumination geometry. The water-leaving radiance has units of W m^{-2} nm^{-1} sr^{-1}.

A.1.1. Normalized water-leaving radiance

The normalized water-leaving radiance (Gordon and Clark, 1981; Morel and Gentili, 1996) is defined as

$$L_{wn}(\lambda, \Omega) = \frac{L_w(\lambda, \Omega)}{t_{\mathrm{down}}(\lambda)\mu_S C_s} \tag{20}$$

where t_{down} is the total downward transmittance of the atmosphere, μ_S is the cosine of the solar zenith angle, and C_s is a coefficient accounting for the variation in the sun-Earth distance. $L_{wn}(\theta_v, \theta_S, \Delta\phi)$ represents the water-leaving radiance that would occur if the atmospheric attenuation were negligible, the sun was at the zenith and at the mean sun-Earth distance. The normalized water-leaving radiance is expressed in units of W m^{-2} nm^{-1} sr^{-1}.

A.1.2. The water reflectance

The water reflectance is the ratio of the water-leaving radiance to the incident solar illumination. It normalizes emerging light by the solar and atmospheric variation:

$$\rho_w(\lambda, \Omega) = \frac{\pi L_{wn}(\lambda, \Omega)}{F_0(\lambda)} \quad \text{or} \quad \rho_w(\lambda, \Omega) = \pi \frac{L_w(\lambda, \Omega)}{t_{\mathrm{down}}(\lambda) F_0(\lambda) \mu_s C_s} \ , \tag{21}$$

with $F_0(\lambda)$ indicating the mean extraterrestrial solar spectral irradiance (in W m^{-2} nm^{-1}). The water reflectance is dimensionless.

A.1.3. Remote-sensing reflectance

The remote sensing reflectance $R_{\mathrm{rs}}(\lambda, \theta_s, \theta_v, \Delta\phi)$ is the ratio of the water-leaving radiance to the incident downward irradiance at the sea surface level:

$$R_{\mathrm{rs}}(\lambda,\Omega) \equiv \frac{L_{\mathrm{w}}(\lambda,\Omega)}{E_{\mathrm{d}}(\lambda,0^{+},\theta_{\mathrm{s}})} \quad , \tag{22}$$

where E_{d} is the downward irradiance and 0^{+} indicates that the measurement is performed just above the sea surface. The downward irradiance $E_{\mathrm{d}}(\lambda,0^{+},\theta_{\mathrm{s}})$ can be also expressed as

$$E_{\mathrm{d}}(\lambda,0^{+},\theta_{\mathrm{s}}) = t_{\mathrm{down}}\,(\lambda)F_{0}(\lambda)\mu_{s}C_{s}, \tag{23}$$

which permits to reformulate the normalized water reflectance as

$$\rho_{w}(\lambda,\Omega) = \pi\frac{L_{\mathrm{w}}(\lambda,\Omega)}{E_{\mathrm{d}}(\lambda,0^{+},\theta_{\mathrm{s}})} = \pi R_{\mathrm{rs}}(\lambda,\Omega), \tag{24}$$

and the normalized water-leaving radiance as

$$L_{wn}(\lambda,\Omega) = F_{\mathrm{o}}\frac{L_{\mathrm{w}}(\lambda,\Omega)}{E_{\mathrm{d}}(\lambda,0^{+},\theta_{\mathrm{s}})}. \tag{25}$$